Materials Today Physics 36 (2023) 101174

Contents lists available at ScienceDirect

Materials Today Physics

journal homepage: www.journals.elsevier.com/materials-today-physics

Porosity and tortuosity: Keys for accurate modeling of porous electrodes in supercapacitors

Shouze Li [a], Zhou Li [a], Dongyan Xu [b], Guang Feng [a], Run Hu [a,*]

[a] School of Energy and Power Engineering, Huazhong University of Science and Technology, Wuhan, 430074, China
[b] Department of Mechanical and Automation Engineering, The Chinese University of Hong Kong, Shatin, New Territories, Hong Kong, Special Administrative Region, China

ARTICLE INFO

Keywords:
Capacitors
Porous electrodes
Porosity
Tortuosity
Equivalent circuit

ABSTRACT

Modeling of porous electrodes in supercapacitors (SCs) is rather important for both characterizing and improving the charging/discharging process of SCs, but the current models fail to balance accuracy, flexibility, and detail characterization of the electrode structure, especially the porosity and tortuosity. In this work, we develop a porous tortuous electrode (PTE) model consisting of a stack of multiple parallel plate capacitors with adjustable structural parameters for accurate modeling of SCs. By solving the equivalent circuit of the PTE model, the influence of the electrode structures on electric capacity and relaxation time are characterized with experimental validation, signifying the keys for accurate modeling of SCs as tortuosity and porosity and offering a general formula for describing the relaxation time of SCs. Based on the adjustable parameters in the PTE model, the spatial heterogeneity of the electrodes enables more intricate electrode structure designs. The PTE model facilitates various electrode designs and provides insight into the charging and discharging kinetics of porous electrodes.

1. Introduction

Supercapacitors (SCs) store energy through the inherent electrical double layers (EDLs) at the electrode-electrolyte interface when an external voltage is applied [1,2] and unlike the redox reaction-based batteries, can function at high charge/discharge rates in almost infinite cycles [2–7]. The local microscopic structures of the electrodes play a crucial role in the energy density and charge/discharge rate of the SCs. On the one hand, the specific surface area of the electrode determines the amount of EDL that SCs can hold [8–10], and on the other hand the pore structure of the electrode affects the diffusion of ions and the charging/discharging time of SCs [10–13]. To optimize the performance of SCs through rational design, it is necessary to accurately define how the electrode morphology influences the relaxation time τ of ionic response under electrode potential Φ and the available capacitance C_s of the SCs [14–16].

Microscopically, people have employed molecular dynamics [17–21], lattice Boltzmann simulations, or classical density generalization theory [22–24], to depict the microscopic interaction of ions and nanopores on the electrode surfaces, but the predicted *ns* timescales are much smaller than the experimental 10^3 s timescales of the experimental SCs because their typical simulation domains are much smaller than the SC thickness ($2L + 2H$) [25]. On the contrary, the macroscale transmission line (TL) models were developed to fit the experimental data, but it is too coarse to reveal the microscopic mechanism of SCs. Moreover, the relaxation time in the TL model is calculated as $\tau_{RC} = \lambda_D L/D$ [26–29], where L is half the length of the electrode separation distance, D is the ionic diffusion coefficient, and λ_D is the Debye length $\lambda_D = \kappa^{-1} = (\varepsilon k_B T/2e^2\rho_b)^{-1/2}$ with ε the electrolyte permittivity, e the elementary charge, k_B the Boltzmann constant, T the cell temperature, and $2\rho_b$ the bulk ion number density [30,31]. Substituting the typical experimental parameters in Ref. [32], the relaxation time in the TL model approximates 10^{-4} s, which is almost 5 orders of magnitude smaller than the experimental relaxation time. To remedy the shortcomings of the TL model, Lian et al. developed the microscopic stack-electrode (SE) model and SE circuit [32] with many no-thickness parallel stacked electrodes to establish the relationship between the parameters in the TL models and electrode structures (pore size h, thickness H, etc.), and obtained the relaxation time that is at the same order of the experimental relaxation time as $\tau_n \sim (2 + 0.75H/L)n\tau_{RC}$ where n is the number of branches. Through their SE model, the slow charging and discharging dynamics in large capacitors could be explained, and the quantitative mechanism under the cyclic voltammetry (CV) is clarified [33].

* Corresponding author.
E-mail address: hurun@hust.edu.cn (R. Hu).

https://doi.org/10.1016/j.mtphys.2023.101174
Received 9 May 2023; Received in revised form 9 July 2023; Accepted 16 July 2023
Available online 21 July 2023

Actually, porous electrodes are frequently used in capacitors [34], lithium/sodium batteries [35,36], and fuel cells [37] among others, due to the large specific surface area supplied by their microporous structure. Some key statistics describing the microstructure of the electrode mainly include porosity, distribution of pore size, and tortuosity [38], etc. The porosity P is the ratio of the pore volume to the total volume of the electrode ($P \leq 1$) as shown in Fig. 1(a). The tortuosity, which is a crucial factor in correctly describing ion diffusion behavior, is defined as the ratio between the average travel distance and the macroscopic distance in porous electrodes ($\gamma \geq 1$). Nevertheless, the lack of practical microstructure parameters of the electrode renders the SE model inaccurate. Hence, detailed characterization of electrode microstructure with more parameters is still lacking for accurate modeling of porous electrodes in SCs yet.

To tackle the above question, we develop a porous tortuous electrode (PTE) model of SCs by considering tortuosity γ and porosity P, whose influences are found to be dominant for the accurate modeling of SCs' performance. The influences of the electrodes' tortuosity and porosity on electric capacity and relaxation time are characterized. The PTE model is validated with previous experiments with higher accuracy than the SE model. Unlike the SE model, the PTE model allows for designing more complex spatial heterogeneity for electrodes to achieve superior performance. The PTE model enables the more general electrode design and the accurate prediction of the charging and discharging kinetics in SCs.

2. Porous tortuous electrode (PTE) model

The PTE model assumes that the contact surface between the electrode and the electrolyte is large enough to neglect the edge effect and to focus on the ion distribution perpendicular to the contact surface. According to Fig. 1(b), the capacitor cathode and anode are composed of n flat electrodes that can be permeated by the electrolyte. The distance between the i-th flat electrode and the (i+1)-th flat electrode is determined by the pore size h_i ($i = \{1, 2, \ldots, n-1\}$ represent the i-th intervals close to the electrolytic cell and the spatial information of branch). By definition of porosity, we can get the average porosity $P_{avg} = \sum h_i/H$ and $n = P_{avg}H/h_{avg} + 1$ (the subscript avg represents the arithmetic mean). The electrode material is designed as a tortuous porous structure consisting of solid particles, which limits the diffusion coefficient of ions in the electrode as $D_{eff,i} = D_{bulk}P_i/\gamma_i$, where D_{eff} and D_{bulk} are effective and bulk diffusion coefficients, respectively. The model can be numerically solved by the Poisson-Nernst-Planck (PNP) equations [39,40], which are relatively complicated and cumbersome. Instead, it could be alternatively solved by calculating the equivalent circuit of the PTE model [Fig. 1(c)], in which the microphysical quantities are converted into resistance and capacitance as

$$C = A\varepsilon\kappa \tag{1a}$$

$$\begin{cases} R_i = \dfrac{h_i}{A\varepsilon\kappa^2 D_{eff,i}} = \dfrac{h_i\gamma_i}{h_{avg}P_i} \times \dfrac{h_{avg}}{A\varepsilon\kappa^2 D} = \dfrac{1}{K_i} \times R \\ R' = \dfrac{2L}{A\varepsilon\kappa^2 D} \end{cases} \tag{1b}$$

where A is the electrode surface area. It is worth noting that the capacitance of the two outermost capacitors in the circuit is half that of the other capacitors because they only have one side to interact with electrolytes [32]. For the circuit on the right side of Fig. 1(c) by $Q = C\Phi$ we could get:

$$\begin{cases} I_1 = \dot{Q}_1 = 2C\Delta\dot{\Phi}_1 \\ \vdots \\ I_{n-1} = \dot{Q}_{n-1} = 2C\Delta\dot{\Phi}_{n-1} \\ I_n = \dot{Q}_n = C\Delta\dot{\Phi}_n \end{cases} \tag{2}$$

In the scope of this work, we consider capacitance C as a constant

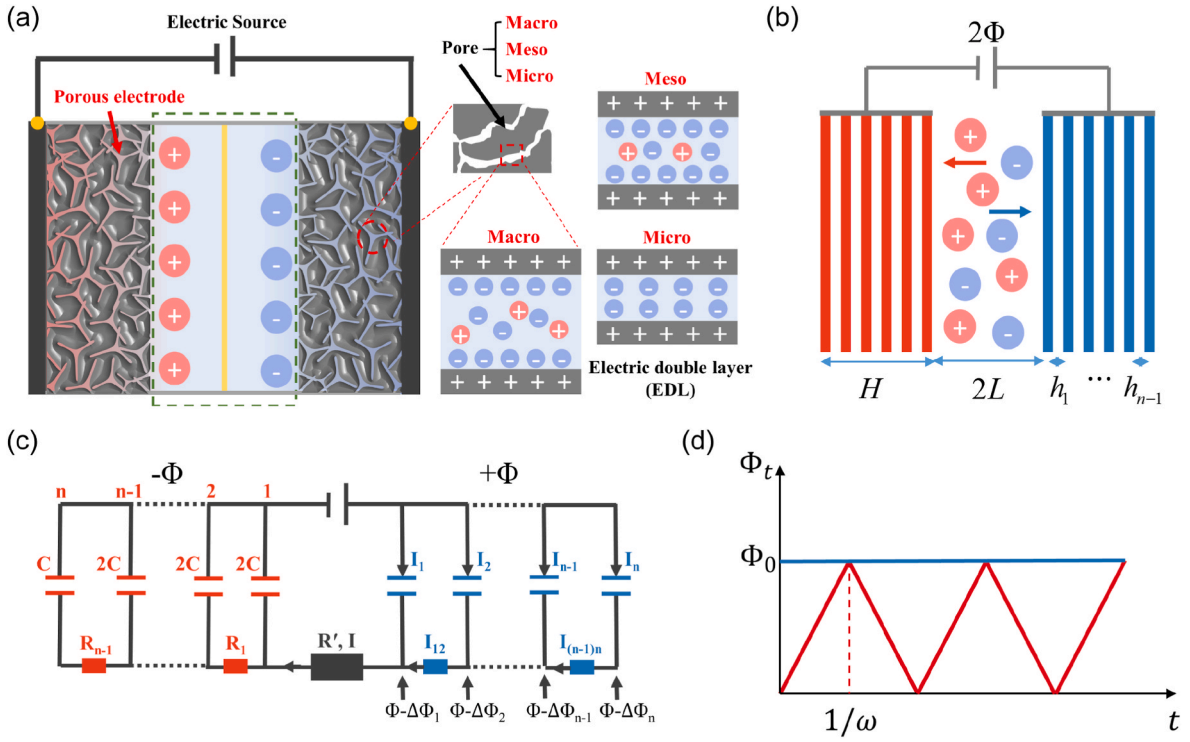

Fig. 1. (a) Schematic diagram of a supercapacitor, containing two symmetrical porous electrodes and an electrolyte cell. (b) Model sketch, the electrolytic cell length 2L. Two electrodes of thickness H are both considered to be composed of $n \geq 1$ flat sheets electrode and the interval between the i-th and the (i+1)-th flat sheets electrode is h_i ($1 \leq i \leq n-1$). (c) The equivalent electronic circuit of the model with a single side connected in parallel by n capacitors, where $R_i \sim h_i$ and $R' \sim 2L$. (d) As a function of voltage Φ(t) - t. (Blue is the constant potential, and red is the sawtooth potential change that is used in CV experiments.). (For interpretation of the references to colour in this figure legend, the reader is referred to the Web version of this article.)

value. The currents in the different branches are related by Kirchhoff's law:

$$\begin{cases} I = I_1 + I_{12} \\ \vdots \\ I_{(n-2)(n-1)} = I_{(n-1)} + I_{(n-1)n} \\ I_{(n-1)n} = I_n \end{cases} \tag{3}$$

The currents through the resistors follow Ohm's law:

$$\begin{cases} IR^{'} = 2[\Phi(t) - \Delta\Phi_1(t)] \\ I_{12}R_1 = \Delta\Phi_1(t) - \Delta\Phi_2(t) \\ \vdots \\ I_{(n-1)n}R_{n-1} = \Delta\Phi_{n-1}(t) - \Delta\Phi_n(t) \end{cases} \tag{4}$$

Combining Eqs. (2)–(4), we get n coupled ordinary differential equations:

$$\begin{cases} \Delta\dot{\Phi}_1(t) = \dfrac{I - I_{12}}{2C} = \dfrac{\Phi(t)}{R^{'}C} - \left(\dfrac{1}{R^{'}C} + \dfrac{1}{2R_1C}\right)\Delta\Phi_1(t) - \dfrac{\Delta\Phi_2(t)}{2R_1C} \\ \vdots \\ \Delta\dot{\Phi}_{n-1}(t) = \dfrac{I_{(n-2)(n-1)} - I_{(n-1)n}}{2C} = \dfrac{\Phi_{n-2}(t)}{2R_{n-2}C} - \left(\dfrac{1}{2R_{n-2}C} + \dfrac{1}{2R_{n-1}C}\right)\Delta\Phi_{n-1}(t) - \dfrac{\Delta\Phi_n(t)}{2R_{n-1}C} \\ \Delta\dot{\Phi}_n(t) = \dfrac{I_n}{C} = \dfrac{\Phi_{n-1}(t)}{R_{n-1}C} - \dfrac{\Phi_n(t)}{R_{n-1}C} \end{cases} \tag{5}$$

We then rewrite Eq. (5) in the matrix form

$$\begin{pmatrix} \Delta\dot{\Phi}_1(t) \\ \Delta\dot{\Phi}_2(t) \\ \vdots \\ \Delta\dot{\Phi}_n(t) \end{pmatrix} = \frac{\Phi(t)}{R^{'}C}\begin{pmatrix} 1 \\ 0 \\ \vdots \\ 0 \end{pmatrix} - \frac{1}{2RC}\begin{pmatrix} K_1 + \dfrac{h_{avg}}{L} & -K_1 & & & \\ -K_1 & K_1 + K_2 & -K_2 & & \\ & \ddots & \ddots & \ddots & \\ & & -K_{n-2} & K_{n-2} + K_{n-1} & -K_{n-1} \\ & & & -2K_{n-1} & 2K_{n-1} \end{pmatrix}\begin{pmatrix} \Delta\Phi_1(t) \\ \Delta\Phi_2(t) \\ \vdots \\ \Delta\Phi_n(t) \end{pmatrix}$$

which can be rewritten as $\Delta\dot{\Phi} = \mathbf{V} - \mathbf{M}\Delta\Phi$ with $\mathbf{\Delta\Phi} = [\Delta\Phi_1, \Delta\Phi_2, \cdots, \Delta\Phi_n]^{\mathrm{T}}$, $\mathbf{V} = [\Phi(t)/R^{'}C]\mathbf{e_1} \in \mathbb{R}^{n\times 1}$, $\mathbf{e_1} = [1,0,0,\cdots,0]^{\mathrm{T}}$ and $\mathbf{M} \in \mathbb{R}^{n\times n}$ is a tridiagonal matrix [32]. Combining the above differential equations and the initial condition $\mathbf{\Delta\Phi}(t=0) = \mathbf{0}$, the solution is

$$\Delta\Phi(t) = \frac{\mathbf{e_1}}{R^{'}C}\int_0^t \Phi(s)\exp[(s-t)\mathbf{M}]\,\mathrm{d}s \tag{6}$$

By eigenvalue decomposition of $\mathbf{M}$ as $\mathbf{M} = \mathbf{U\Lambda U}^{-1}$ with $\mathbf{U}$ the unitary matrix and $\mathbf{\Lambda} = \mathrm{diag}(\lambda_1, \lambda_2, \cdots, \lambda_n)$ the eigenvalue matrix, we can rewrite Eq. (6) as

$$\Delta\Phi(t) = \mathbf{U}\int_0^t \exp[(s-t)\Lambda]\mathbf{U}^{-1}\mathbf{V}(s)\mathrm{d}s \tag{7}$$

In the following, we discuss the integration results for different forms of supply voltage such as constant voltage charging (blue line) and sawtooth CV scan (red line) in Fig. 1(d).

Case 1. constant voltage charging:

For this case, the power supply voltage is constant as

$$\Phi(t) = \Phi_0(t > 0), \tag{8}$$

so $\mathbf{V} = [\Phi_0/R^{'}C]\mathbf{e_1}$. Integrating Eq. (7) gives:

$$\Delta\Phi(t) = \frac{\Phi_0}{R^{'}C}\mathbf{U}[1 - \exp(-t\Lambda)]\Lambda^{-1}\mathbf{U}^{-1}\mathbf{e_1}. \tag{9}$$

As described in Eq. (9), each voltage at branch capacitance drops exponentially with time and has different relaxation times $1/\lambda_i$, which helps us subsequently to solve the overall relaxation time of the PTE model. By inserting Eq. (9) into Eq. (2), we can obtain the current in each branch as

$$\mathbf{I}(t) = \frac{\Phi_0}{R^{'}}\mathbf{SU}\exp(-t\Lambda)\mathbf{U}^{-1}\mathbf{e_1} \quad \text{and} \quad \mathbf{S} = \begin{pmatrix} 2 & & & \\ & 2 & & \\ & & \ddots & \\ & & & 1 \end{pmatrix} \tag{10}$$

Case 2. sawtooth CV scan:

Let u be the number of cycle periods, for a periodic sawtooth potential, it can be expressed as:

$$\Phi(t) = \Phi_0(1 - |\omega t - 2u - 1|) \tag{11}$$

We perform a Fourier series expansion of $\Phi(t)$ to make it continuous and integrable:

$$\Phi(t) = \Phi_0\left[\frac{1}{2} - \frac{4}{\pi^2}\sum_{m=1,3,5,\cdots}^{\infty}\frac{\cos(m\pi\omega t)}{m^2}\right] \tag{12}$$

By inserting Eq. (12) into Eq. (7), we find:

$$\Delta\Phi(t) = \frac{\Phi_0}{R^{'}C}\mathbf{U}\mathrm{diag}(\alpha_1, \cdots, \alpha_n)\mathbf{U}^{-1}\mathbf{e_1} \tag{13}$$

where α_i is defined as:

$$\begin{cases} \alpha_i \equiv \alpha_i^0 - \dfrac{4}{\pi^2}\displaystyle\sum_{m=1,3,5,\cdots}^{\infty}\frac{\alpha_i^{\cos}}{m^2} \\ \alpha_i^0 \equiv \dfrac{1 - \exp(-\lambda_i t)}{2\lambda_i} \\ \alpha_i^{\cos} \equiv \displaystyle\int_0^t \cos(m\pi\omega s)\exp[(s-t)\lambda_i]\,\mathrm{d}s \end{cases} \tag{14}$$

Here, α_i^0 stems from the term 1/2 in Eq. (12). For the solution of $\alpha_i^{\cos}$:

$$\begin{aligned} \alpha_i^{\cos} &= \int_0^t \cos(m\pi\omega s)\exp[(s-t)\lambda_i]\,\mathrm{d}s \\ &= \frac{1}{m\pi\omega}\int_0^t \exp[(s-t)\lambda_i]\,\mathrm{d}\sin(m\pi\omega s) \\ &= \frac{1}{m\pi\omega}\left\{\sin(m\pi\omega t) - \int_0^t \sin(m\pi\omega s)\,\mathrm{d}\exp[(s-t)\lambda_i]\right\} \\ &= \frac{1}{m\pi\omega}\left\{\sin(m\pi\omega t) + \frac{\lambda_i}{m\pi\omega}\int_0^t \exp[(s-t)\lambda_i]\,\mathrm{d}\cos(m\pi\omega s)\right\} \\ &= \frac{1}{m\pi\omega}\left\{\sin(m\pi\omega t) + \frac{\lambda_i}{m\pi\omega}\left[\cos(m\pi\omega t) - \exp(-\lambda_i t) - \lambda_i\alpha_i^{\cos}\right]\right\} \end{aligned}$$

Thus, we obtain the final solution of $\alpha_i^{\cos}$ as:

$$\alpha_i^{\cos} = \frac{(m\pi\omega)\sin(m\pi\omega t) + \lambda_i \cos(m\pi\omega t) - \lambda_i \exp(-\lambda_i t)}{\lambda_i^2 + (m\pi\omega)^2} \tag{15}$$

We ignore the transient response in Eq. (14) and Eq. (15) when t is large enough and obtain

$$\alpha_i = \frac{1}{2\lambda_i} - \frac{4}{\pi^2} \sum_{m=1,3,5,\cdots}^{\infty} \frac{1}{m^2} \frac{(m\pi\omega)\sin(m\pi\omega t) + \lambda_i \cos(m\pi\omega t)}{\lambda_i^2 + (m\pi\omega)^2} \tag{16}$$

Inserting Eq. (16) into Eq. (2), we get

$$\mathbf{I}(t) = \frac{\Phi_0}{R} \mathbf{S}\mathbf{U}\mathrm{diag}(\beta_1, \cdots, \beta_n)\mathbf{U}^{-1}\mathbf{e_1} \tag{17}$$

with β_i given by

$$\beta_i = \frac{\mathrm{d}\alpha_i}{\mathrm{d}t} = \frac{4}{\pi^2} \sum_{m=1,3,5,\cdots}^{\infty} \frac{1}{m^2} \frac{\lambda_i(m\pi\omega)\sin(m\pi\omega t) - (m\pi\omega)^2 \cos(m\pi\omega t)}{\lambda_i^2 + (m\pi\omega)^2} \tag{18}$$

So the dry circuit current is $J(t) = \sum I_i(t)$. Here, we mainly focus on the effect of microscopic parameters P_i and γ_i of electrodes on SCs, which haven't been investigated before. Further, by adjusting different functions of the supply potential $\Phi(t)$, we examine how the PTE model responds to various electrochemical tests, such as the constant potential technique and CV test, and analyze the correlation between electrode parameters and SC performance.

We validated the PTE model with experimental results in Ref. [41]. We extract the electrode parameters from the experimental results as cell dimension $H = 40$ μm and $2L = 150$ μm. The electrolyte is 0.5 M Na_2SO_4 at room temperature, the bulk diffusion coefficient is $D_{\mathrm{bulk}} = 1.23 \times 10^{-9}$ m^2/s, and the Debye length is $\lambda_D = \kappa^{-1} = 0.25$ nm. The selection of h_i is constructed according to the pore size distribution obtained from the N_2 adsorption/desorption test of Ref. [41]. The cumulative pore capacity is $V_{\mathrm{pore}} = 2.8\ \mathrm{cm}^3/\mathrm{g}$ [41]and the corresponding porosity is $P = V_{\mathrm{pore}}\rho = 0.52$. The Bruggeman's correlation is widely employed in engineering for roughly estimating tortuosity due to the inherent difficulty in directly accessing tortuosity. So the tortuosity of the electrode is estimated by Bruggeman's correlation as $\gamma = P^{-0.5} \approx 1.39$ [42,43]. With a constant voltage as $\Phi(t) = \Phi_0(t > 0) = 0.5$ V, the PTE model predicted CV scan curves at the corresponding frequency ω are shown in Fig. 2. The curves predicted by the PTE match the curve of the capacitor's ideal voltammetry, which is rectangular at low scan frequencies and becomes lens-shape at high frequencies due to the ion diffusion limitation [8]. It is seen in Fig. 2 that the PTE predictions (red lines) agree well with the experiments (symbols), while there is a large discrepancy between the SE predictions (orange lines) and the experiments, especially at the low frequency. The discrepancy between the two predictions demonstrates that the porosity and tortuosity play an important role in the model accuracy of energy density (area enclosed by the curve) and relaxation time (shape of the curve).

3. Results and discussions

3.1. Relaxation time

The power density of SC is commonly characterized by the charge relaxation time τ. Here we construct a quantitative relationship between relaxation times and electrode parameters in the PTE model. The overall equilibrium of the capacitor relies on the equilibrium of its individual branches according to Eq. (9). Fig. 3(a) illustrates the temporal change of normalized charge in each electrode branch during constant voltage charging. Initially, the capacitor primarily charges in the vicinity of the electrolyte and gradually extends towards the outer layer. Notably, the overall change in the capacitor's charge aligns with the change observed in the $i = 41$ branch, which possesses the smallest characteristic value [see Fig. 3(b)]. Stated differently, the relaxation time of the entire capacitor is determined by the longest relaxation time among its branches: $\tau = 1/\min(\lambda_i)$. Now the problem becomes solving the relationship between the minimum eigenvalues and the electrode parameters.

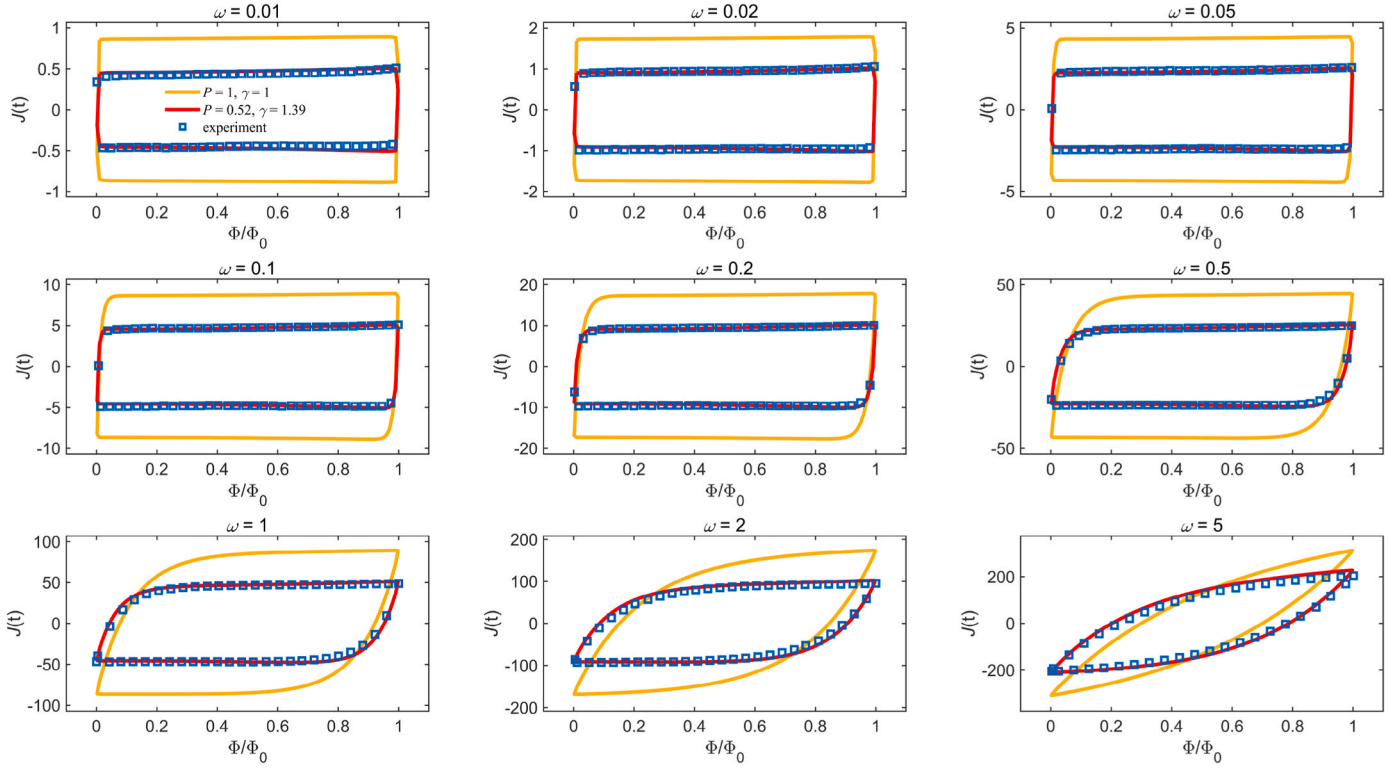

Fig. 2. Validation of the PTE model (red lines: $P_i = 0.52$, $\gamma_i = 1.39$) with experiments in Ref. [41] (symbols) and the SE model (orange lines: Influences of porosity and tortuosity are ignored as $P_i = 1.0$, $\gamma_i = 1.0$) with $\Phi_0 = 0.5$ V at different frequencies ω. (For interpretation of the references to colour in this figure legend, the reader is referred to the Web version of this article.)

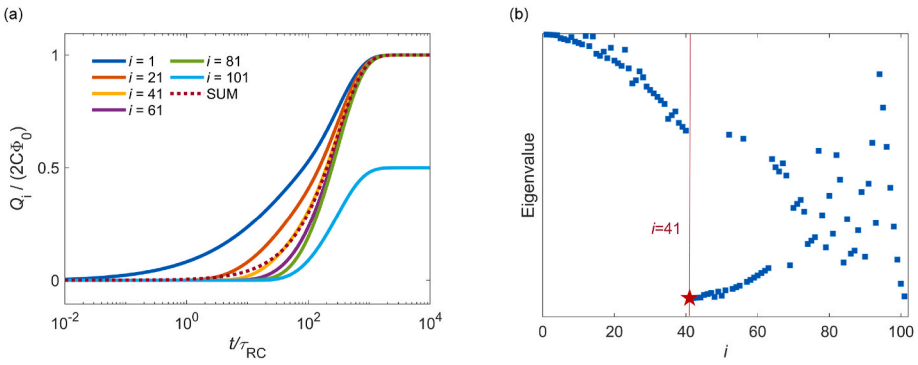

Fig. 3. (a) Normalized charge of each branch of the electrode's constant voltage charging (Calculate by Eq. (2) and Eq. (10)) with $\Phi_0 = 0.5$ V, $h_i = 10$ nm, $H/L = 1$, $H = 1$ μm, $P_i = 0.6$, and $\gamma_i = 1.4$. (b) Eigenvalue of each branch in (a). The asterisk denotes the smallest eigenvalue.

For simplicity, let's assume $h_i \equiv h_{avg}$, $P_i \equiv P$, and $\gamma_i \equiv \gamma$, implying $K_i = P/\gamma$. Consequently, the characteristic matrix **M** of the electrode model can be represented as follows:

$$\mathbf{M} = \frac{1}{2RC}\begin{pmatrix} K+\frac{h}{L} & -K & & & & \\ -K & 2K & -K & & & \\ & \ddots & \ddots & \ddots & & \\ & & -K & 2K & K & \\ & & & -2K & 2K & \end{pmatrix} = \frac{(n-1)L}{PHRC}\begin{pmatrix} \frac{P}{\gamma}+\frac{PH}{(n-1)L} & -\frac{P}{\gamma} & & & & \\ -\frac{P}{\gamma} & 2\frac{P}{\gamma} & -\frac{P}{\gamma} & & & \\ & \ddots & \ddots & \ddots & & \\ & & -\frac{P}{\gamma} & 2\frac{P}{\gamma} & -\frac{P}{\gamma} & \\ & & & -2\frac{P}{\gamma} & 2\frac{P}{\gamma} & \end{pmatrix} = \frac{(n-1)L}{2H\tau_{RC}}\begin{pmatrix} \frac{1}{\gamma}+\frac{H}{(n-1)L} & -\frac{1}{\gamma} & & & & \\ -\frac{1}{\gamma} & 2\frac{1}{\gamma} & -\frac{1}{\gamma} & & & \\ & \ddots & \ddots & \ddots & & \\ & & -\frac{1}{\gamma} & 2\frac{1}{\gamma} & -\frac{1}{\gamma} & \\ & & & -2\frac{1}{\gamma} & 2\frac{1}{\gamma} & \end{pmatrix} \quad (19)$$

By solving the eigenvalues of Eq. (19), we can obtain the relaxation time τ, which is influenced by τ_{RC}, H/L, n, and γ. To quantitatively illustrate the influence, we plotted the relaxation time as a function of each parameter in Fig. 4(a–d). It is seen that there is a good linear relationship between τ and τ_{RC}, H/L, n, γ respectively. So τ can be accurately approximated as a linear combination of τ_{RC}, H/L, n, γ:

$$\tau = \tau_{RC}\left(a\gamma\frac{H}{L}n + b_1\gamma\frac{H}{L} + b_2\gamma n + b_3\frac{H}{L}n + c_1\gamma + c_2\frac{H}{L} + c_3 n + d\right) \quad (20)$$

when $H/L \to 0$, implying $R/R' \to 0$, all branch capacitors are connected in parallel, giving a total capacitance $C_{total} = (2n\text{-}1)C$. Inserting this into $\tau = R'C_{total}/2$, we find: $\tau = (2n\text{-}1)R'C/2 = (2n\text{-}1)\tau_{RC}$, resulting in $b_2 = c_1 = 0$, $c_3 = 2$, $d = -1$ when compared with Eq. (21). Thus Eq. (21) is simplified as:

$$\frac{\tau}{\tau_{RC}} = \left(a\frac{H}{L}n + b_1\frac{H}{L}\right)\gamma + \left(b_3\frac{H}{L}n + c_2\frac{H}{L} + 2n - 1\right) = coeff_k \cdot \gamma + coeff_b \quad (21)$$

By performing a 3-dimensional linear fitting of the calculated data in Fig. 4(e and f), we can obtain

$$\frac{\tau}{\tau_{RC}} = 0.8\gamma\frac{H}{L}n - 0.81\gamma\frac{H}{L} - 0.05\frac{H}{L}n - 0.1\frac{H}{L} + 2n + 1 \quad (22)$$

For general SCs, Eq. (22) can be simplified as $\tau \sim (2 + 0.8\gamma H/L\text{-}0.05H/L)n\tau_{RC} \approx (2 + 0.8\gamma H/L\text{-}0.05H/L)(PH/h)\tau_{RC}$ due to $n \gg 1$.

We applied Eq. (22) to the experiment to test the accuracy. Here we consider the setup in Ref. [44]. For the overall dimensions, the thickness of the carbon electrode $H = 0.5$ mm and separator $2L = 2.2$ mm, so $H/L = 0.45$. The electrode is submerged in 1 M NaCl solution at room temperature with bulk diffusion coefficient $D_{bulk} = 1.6 \times 10^{-9}$ m^2/s and Debye length $\kappa^{-1} = 0.3$ mm, thus RC relaxation time is $\tau_{RC} = 2.06 \times 10^{-4}$ s. For the microstructure of the electrode, porosity $P_i = 0.65$, mass density $\rho = 5.8 \times 10^5$ g/m^3, and Brunauer-Emmett-Teller area $A_{BET} = 1330$ m^2/g from nitrogen adsorption, thus average pore size is estimated as $h_{avg} = P/(\rho A_{BET}) = 0.84$ nm and $n = PH/h_{avg} + 1 = 3.87 \times 10^5$. The tortuosity of the electrode is estimated using Bruggeman's correlation as $\gamma_i = P_i^{-0.5} = 1.24$ [42,43,45,46]. With Eq. (22), we find $\tau = 193$ s, which gets the same magnitude as the relaxation time $\tau_{fit} = 200$ s obtained by fitting the experimental data [32,44]. Such small errors are acceptable for guiding structural design.

3.2. Capacitance

The energy density of SC can be characterized by the capacitance value C_s. The CV scanning results at different parameters and scanning frequencies [Fig. 5] are computed and subsequently converted into the electrode's equivalent surface capacitance C_s

$$C_s = \oint \frac{J(t)}{2\Phi_0^2\omega}\mathrm{d}\Phi. \quad (23)$$

For the effect of tortuosity, the equivalent surface capacitance of each curve is equal at low scan frequencies ($\tau\omega \to 0$) as shown in Fig. 5 (a). The tortuosity does not affect parameter n, which implies that varying the tortuosity will not impact the number of EDLs that can be formed. Therefore, it does not affect the maximum energy density and maximum surface capacitance $C_{s,max} = (2n\text{-}1)C$. At high frequencies, SCs with small tortuosity γ_i electrodes can maintain larger equivalent surface capacitance C_s, which depends on the smaller relaxation time τ in faster ions migration as $D_{eff,i} = D_{bulk}P_i/\gamma_i$.

The effect of porosity P is more complex than that of tortuosity γ. As shown in Fig. 5(b), for the energy density, the maximum surface capacitance is proportional to porosity P [Fig. 5(b-c)], whi ch can be explained by $C_{s,max} = (2n\text{-}1)C = (2P_{avg}H/h_{avg} + 1)C$. Increasing porosity allows the electrode to create a greater number of EDLs and store a higher amount of energy. However, this advantage often comes at the cost of extended relaxation time. Fortunately, larger porosity also permits faster ion migration rates, thus the charge/discharge rate is affected by the combination of layer number change and ions diffusion change

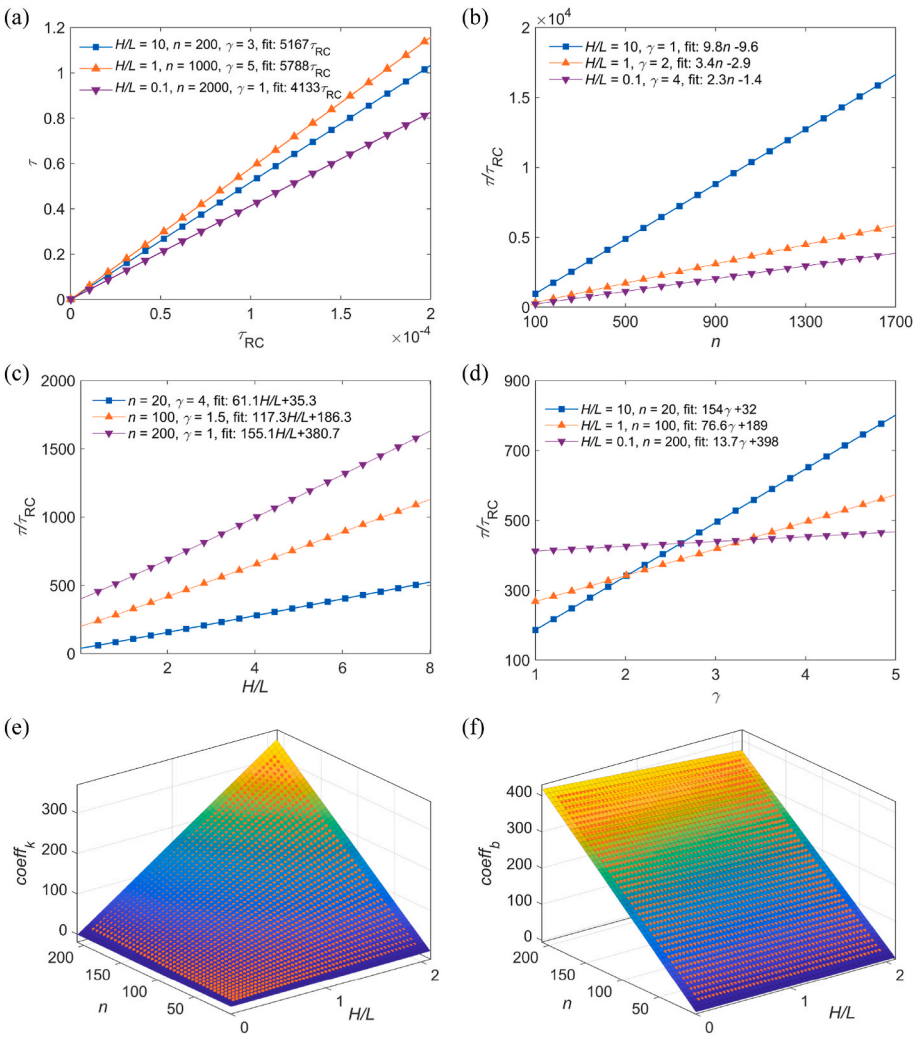

Fig. 4. (a–d) Variation of relaxation time τ [calculated by $\tau = 1/\min(\lambda_i)$] with RC relaxation time τ_{RC}, number of branches n, ratio H/L, tortuosity γ under different conditions. (e–f) The 3-dimensional fit of $coeff_k$ and $coeff_b$, where points are data points and faces are fitted surfaces. The goodness-of-fit of $coeff_k$ and $coeff_b$, respectively, are $R_k^2 = 0.999$ and $R_b^2 = 0.997$.

due to the change of P.

According to Eq. (22), the scan rate ω is rescaled by the relaxation time τ of the electrode model response step potential and the variation of the dimensionless surface capacitance can be represented as the same curve [Fig. 5(d)]:

$$C_s^* = \frac{1}{1 + 6.07(\omega\tau)^{1.4}} \tag{24}$$

Inserting Eq. (24) into $C_s = C^* sC_{s,max}$, we get

$$C_s = \frac{(2n-1)C}{1 + 6.07(\omega\tau)^{1.4}} \tag{25}$$

Combining Eq. (22), Eq. (25) and $n = P_{avg}H/h_{avg} + 1$ gives $C_s \propto AP/[1 + B(\omega P)^{1.4}]$. Therefore, the resulting larger C_s for electrodes with small porosity at $\omega \geq 2.5 \times 10^3$ Hz in Fig. 5(c) can be explained by the enhanced influence of relaxation time at higher frequencies compared to lower frequencies.

3.3. Inhomogeneous electrode design

Although the majority of electrodes can be categorized as homogeneous electrodes, the present PTE model is also applicable for electrodes with inhomogeneous spatial distribution, which have been proven to be an effective way to improve SCs performance [47,48]. Without loss of generality, we discuss a simple case with a stepwise spatial distribution of pore size or porosity characterized by coefficient r as shown in Fig. 6 (a). As shown in Fig. 6(b), the relaxation time τ and r have a negative linear/non-monotonic correlation in the stepwise distribution of h_i/P_i, respectively, which is consistent with Ref. [49]. This phenomenon can be explained by the resistance R_i. The resistance R_i on the inner side is smaller as the electrode near the electrolyte side has a smaller pore size and larger porosity. As a result, the bulk ions can diffuse into the electrode more quickly than the uniform distribution of electrodes during charging and discharging. However, the effect of porosity distribution is different from that of pore size distribution. In stepwise spatial distribution of P_i, the total impedance rises with the increase of $|r|$, which is noteworthy when P_{avg} is large. Therefore, the change of relaxation time in Fig. 6(b) is non-monotonic and asymmetric due to the combined effects of both actions. The CV tests in Fig. 6(c and d) show that the relaxation time of the electrode with the pore size h_i stepwise distribution at $r = 0.8$ is reduced by 20% and the C_s*-ω curve of the designed electrode is between the initial curve and the curve obtained from Eq. (24).

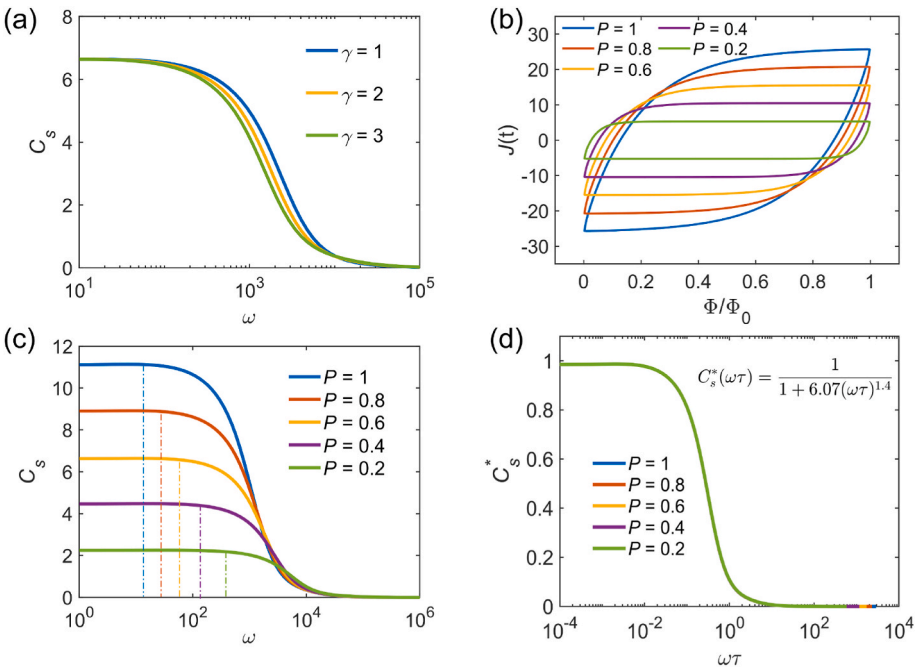

Fig. 5. CV scan of electrodes with $\Phi_0 = 0.01$ V, $h_i = 10$ nm, $H/L = 1$, $H = 2$ μm. (a) $P_i = 0.6$ with different γ_i. (b) CV scan of electrodes with different porosity and $\gamma_i = 2$, $\omega = 400$ Hz. (c) The equivalent surface capacitance of the electrodes in (b) at different scanning frequencies. (d) The dimensionless surface capacitance of the electrode $C_s^* = C_s/C_{s,\max}$ in (c) varies with $\tau\omega$ (τ is calculated by Eq. (22)).

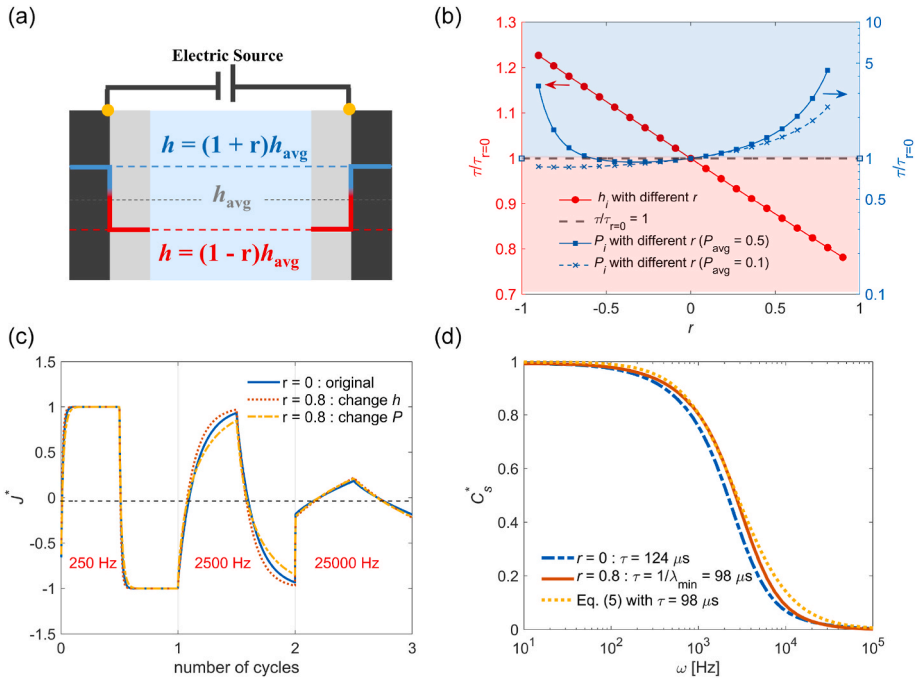

Fig. 6. (a) Schematic diagram of the stepwise spatial distribution of h_i or P_i where $h_i = (1\text{-}r)h_{avg}$ at $i = 1, 2, \ldots, (n\text{-}1)/2$ and $h_i = (1+r)h_{avg}$ at $i = (n+1)/2, \ldots, n\text{-}1$. (b) Effect of changing r in stepwise distribution on relaxation time (Bruggeman's correlation was applied to estimate the tortuosity). (c) Dimensionless current density response of stepwise distributed electrodes in cyclic voltammetry with variable frequency. (d) Change of C_s^* with frequency in h_i stepwise distribution with $r = 0.8$.

4. Conclusions and outlooks

In summary, we built the PTE model to investigate the effect of nanopore structure on the SCs. The corresponding equivalent circuit models were constructed by the structural parameters of the electrodes including thickness H, pore size h_i, porosity P_i, and tortuosity γ_i. We create a link between the capacitor's energy density, charge/discharge rate and the electrode parameters by concentrating on the impacts of the electrodes' porosity and tortuosity on the EDL capacitors. The important role of porosity and tortuosity in the prediction model and the physical mechanism of their influence are revealed. The relaxation time for a general capacitor with uniform electrodes can be expressed as $\tau \sim (2 + 0.8\gamma H/L - 0.05H/L)(PH/h)\tau_{RC}$. The accuracy of the circuit model was verified in the relaxation time evaluation and cyclic voltammetry results

of recent experimental data. Additionally, the PTE model with more practical parameters enables the spatial pore size/porosity heterogeneity design of electrode structures with higher performance of reduced relaxation time by ~20% at $r = 0.8$. The PTE model facilitates various electrode designs and provides insight into the charging and discharging kinetics of porous electrodes, but more work can be done to further improve the accuracy and generality. For instance, the capacitance C in this study is assumed as constant, which can be influenced by the voltage as $C = A\varepsilon\kappa\cosh(\Phi/2)$. When the voltage is low, the influence is minimal, but the corresponding influence may not be ignored at high voltage although Eq. (23) still maintain. Other limitations like capacitor's ion depletion [50], thermal effect [51], and EDL overlap effect [52] that affects diffusion resistance and energy density are also worthy of further discussion. The solutions to these issues may require multi-scale models to combine the present PTE model, PNP model, and molecular dynamics.

Credit author statement

Shouze Li: Conceptualization, formalism derivation, validation, writing and editing; Zhou Li, Dongyan Xu, Guang Feng: Writing and editing; Run Hu: Conceptualization, writing, reviewing, supervision.

Declaration of competing interest

The authors declare that they have no known competing financial interests or personal relationships that could have appeared to influence the work reported in this paper.

Data availability

Data will be made available on request.

Acknowledgement

The work is supported by National Natural Science Foundation of China (NSFC No. 52161160332). D.X. acknowledges the NSFC/RGC Joint Research Scheme (Project No. N_CUHK419/21) sponsored by the Research Grants Council of the Hong Kong Special Administrative Region, China.

References

[1] J.R. Miller, R.A. Outlaw, B.C. Holloway, Graphene double-layer capacitor with ac line-filtering performance, Science 329 (2010) 1637–1639, https://doi.org/10.1126/science.1194372.
[2] J.R. Miller, P. Simon, Electrochemical capacitors for energy management, Science 321 (2008) 651–652, https://doi.org/10.1126/science.1158736.
[3] J. Chmiola, G. Yushin, Y. Gogotsi, C. Portet, P. Simon, P.L. Taberna, Anomalous increase in carbon capacitance at pore sizes less than 1 nanometer, Science 313 (2006) 1760–1763, https://doi.org/10.1126/science.1132195.
[4] M. Janssen, R. van Roij, Reversible heating in electric double layer capacitors, Phys. Rev. Lett. 118 (2017): 096001, https://doi.org/10.1103/PhysRevLett.118.096001.
[5] P. Simon, Y. Gogotsi, B. Dunn, Where do batteries end and supercapacitors begin? Science 343 (2014) 1210–1211, https://doi.org/10.1126/science.1249625.
[6] Q. Yang, X. Jia, X. Li, Q. Yang, T. Zhang, X. Huang, Q. Zheng, C. Li, J. Shao, Understanding the capacitive charge in bulk porous electrodes by mathematical modeling, Phys. Rev. Appl. 17 (2022): 044045, https://doi.org/10.1103/PhysRevApplied.17.044045.
[7] M. Salanne, B. Rotenberg, K. Naoi, K. Kaneko, P.-L. Taberna, C.P. Grey, B. Dunn, P. Simon, Efficient storage mechanisms for building better supercapacitors, Nat. Energy 1 (2016) 1–10, https://doi.org/10.1038/nenergy.2016.70.
[8] G. Jeanmairet, B. Rotenberg, M. Salanne, Microscopic simulations of electrochemical double-layer capacitors, Chem. Rev. 122 (2022) 10860–10898, https://doi.org/10.1021/acs.chemrev.1c00925.
[9] D.L.Z. Caetano, S.J. de Carvalho, G.V. Bossa, S. May, Monte Carlo simulations and mean-field modeling of electric double layers at weakly and moderately charged spherical macroions, Phys. Rev. E. 104 (2021): 034609, https://doi.org/10.1103/PhysRevE.104.034609.
[10] J. Seebeck, C. Merlet, R.H. Meißner, Elucidating curvature-capacitance relationships in carbon-based supercapacitors, Phys. Rev. Lett. 128 (2022): 086001, https://doi.org/10.1103/PhysRevLett.128.086001.
[11] A.C. Forse, J.M. Griffin, C. Merlet, J. Carretero-Gonzalez, A.-R.O. Raji, N.M. Trease, C.P. Grey, Direct observation of ion dynamics in supercapacitor electrodes using in situ diffusion NMR spectroscopy, Nat. Energy 2 (2017) 1–7, https://doi.org/10.1038/nenergy.2016.216.
[12] D.T. Limmer, C. Merlet, M. Salanne, D. Chandler, P.A. Madden, R. van Roij, B. Rotenberg, Charge fluctuations in nanoscale capacitors, Phys. Rev. Lett. 111 (2013): 106102, https://doi.org/10.1103/PhysRevLett.111.106102.
[13] H.D. Yoo, J.H. Jang, J.H. Ryu, Y. Park, S.M. Oh, Impedance analysis of porous carbon electrodes to predict rate capability of electric double-layer capacitors, J. Power Sources 267 (2014) 411–420, https://doi.org/10.1016/j.jpowsour.2014.05.058.
[14] M. Janssen, Curvature affects electrolyte relaxation: studies of spherical and cylindrical electrodes, Phys. Rev. E. 100 (2019): 042602, https://doi.org/10.1103/PhysRevE.100.042602.
[15] J. Yan, S. Li, B. Lan, Y. Wu, P.S. Lee, Rational design of nanostructured electrode materials toward multifunctional supercapacitors, Adv. Funct. Mater. 30 (2020): 1902564, https://doi.org/10.1002/adfm.201902564.
[16] S. Kondrat, A. Kornyshev, Charging dynamics and optimization of nanoporous supercapacitors, J. Phys. Chem. C 117 (2013) 12399–12406, https://doi.org/10.1021/jp400558y.
[17] C. Péan, C. Merlet, B. Rotenberg, P.A. Madden, P.-L. Taberna, B. Daffos, M. Salanne, P. Simon, On the dynamics of charging in nanoporous carbon-based supercapacitors, ACS Nano 8 (2014) 1576–1583, https://doi.org/10.1021/nn4058243.
[18] S. Kondrat, P. Wu, R. Qiao, A.A. Kornyshev, Accelerating charging dynamics in subnanometre pores, Nat. Mater. 13 (2014) 387–393, https://doi.org/10.1038/nmat3916.
[19] G. Feng, M. Chen, S. Bi, Z.A.H. Goodwin, E.B. Postnikov, N. Brilliantov, M. Urbakh, A.A. Kornyshev, Free and bound states of ions in ionic liquids, conductivity, and underscreening paradox, Phys. Rev. X 9 (2019): 021024, https://doi.org/10.1103/PhysRevX.9.021024.
[20] G. Feng, P.T. Cummings, Supercapacitor capacitance exhibits oscillatory behavior as a function of nanopore size, J. Phys. Chem. Lett. 2 (2011) 2859–2864, https://doi.org/10.1021/jz201312e.
[21] S. Bi, H. Banda, M. Chen, L. Niu, M. Chen, T. Wu, J. Wang, R. Wang, J. Feng, T. Chen, M. Dincă, A.A. Kornyshev, G. Feng, Molecular understanding of charge storage and charging dynamics in supercapacitors with MOF electrodes and ionic liquid electrolytes, Nat. Mater. 19 (2020) 552–558, https://doi.org/10.1038/s41563-019-0598-7.
[22] S. Babel, M. Eikerling, H. Löwen, Impedance resonance in narrow confinement, J. Phys. Chem. C 122 (2018) 21724–21734, https://doi.org/10.1021/acs.jpcc.8b05559.
[23] D. Jiang, J. Wu, Microscopic insights into the electrochemical behavior of nonaqueous electrolytes in electric double-layer capacitors, J. Phys. Chem. Lett. 4 (2013) 1260–1267, https://doi.org/10.1021/jz4002967.
[24] J. Jiang, D. Cao, D. Jiang, J. Wu, Kinetic charging inversion in ionic liquid electric double layers, J. Phys. Chem. Lett. 5 (2014) 2195–2200, https://doi.org/10.1021/jz5009533.
[25] C. Péan, C. Merlet, B. Rotenberg, P.A. Madden, P.-L. Taberna, B. Daffos, M. Salanne, P. Simon, On the dynamics of charging in nanoporous carbon-based supercapacitors, ACS Nano 8 (2014) 1576–1583, https://doi.org/10.1021/nn4058243.
[26] S. Fletcher, V.J. Black, I. Kirkpatrick, A universal equivalent circuit for carbon-based supercapacitors, J. Solid State Electrochem. 18 (2014) 1377–1387, https://doi.org/10.1007/s10008-013-2328-4.
[27] J.H. Jang, S. Yoon, B.H. Ka, Y.-H. Jung, S.M. Oh, Complex capacitance analysis on leakage current appearing in electric double-layer capacitor carbon electrode, J. Electrochem. Soc. 152 (2005) A1418, https://doi.org/10.1149/1.1931469.
[28] M. Janssen, Transmission line circuit and equation for an electrolyte-filled pore of finite length, Phys. Rev. Lett. 126 (2021), https://doi.org/10.1103/PhysRevLett.126.136002.
[29] M. Janssen, M. Bier, Transient dynamics of electric double-layer capacitors: exact expressions within the Debye-Falkenhagen approximation, Phys. Rev. E. 97 (2018): 052616, https://doi.org/10.1103/PhysRevE.97.052616.
[30] M.Z. Bazant, K. Thornton, A. Ajdari, Diffuse-charge dynamics in electrochemical systems, Phys. Rev. E. 70 (2004): 021506, https://doi.org/10.1103/PhysRevE.70.021506.
[31] P.M. Biesheuvel, M.Z. Bazant, Nonlinear dynamics of capacitive charging and desalination by porous electrodes, Phys. Rev. E. 81 (2010): 031502, https://doi.org/10.1103/PhysRevE.81.031502.
[32] C. Lian, M. Janssen, H. Liu, R. van Roij, Blessing and curse: how a supercapacitor's large capacitance causes its slow charging, Phys. Rev. Lett. 124 (2020): 076001, https://doi.org/10.1103/PhysRevLett.124.076001.
[33] Y. Lin, C. Lian, M.U. Berrueta, H. Liu, R. van Roij, Microscopic model for cyclic voltammetry of porous electrodes, Phys. Rev. Lett. 128 (2022): 206001, https://doi.org/10.1103/PhysRevLett.128.206001.
[34] C. Chi, D. Li, Y. Li, X. Qi, H. Huang, Q. Wang, C. Lin, X. Zhang, W. Ma, B. Huang, Silicon-nanoforest-based solvent-free micro-supercapacitors with ultrahigh spatial resolution via IC-compatible in situ fabrication for on-chip energy storage, J. Mater. Chem. A. 8 (2020) 22736–22744, https://doi.org/10.1039/D0TA07540J.
[35] M. Ihsan-Ul-Haq, H. Huang, J. Wu, N. Mubarak, A. Susca, Z. Luo, B. Huang, J.-K. Kim, Unveiling solid electrolyte interface morphology and electrochemical kinetics of amorphous Sb2Se3/CNT composite anodes for ultrafast sodium storage, Carbon 171 (2021) 119–129, https://doi.org/10.1016/j.carbon.2020.09.011.
[36] H. Huang, H.-H. Wu, C. Chi, J. Zhu, B. Huang, T.-Y. Zhang, Out-of-plane ion transport makes nitrogenated holey graphite a promising high-rate anode for both

Li and Na ion batteries, Nanoscale 11 (2019) 18758–18768, https://doi.org/10.1039/C9NR06011A.
[37] T.Z. Sholklapper, H. Kurokawa, C.P. Jacobson, S.J. Visco, L.C. De Jonghe, Nanostructured solid oxide fuel cell electrodes, Nano Lett. 7 (2007) 2136–2141, https://doi.org/10.1021/nl071007i.
[38] J. Santoki, S. Daubner, D. Schneider, M. Kamlah, B. Nestler, Effect of tortuosity, porosity, and particle size on phase-separation dynamics of ellipsoid-like particles of porous electrodes: Cahn–Hilliard-type phase-field simulations, Model. Simul. Mater. Sci. Eng. 29 (2021): 065010, https://doi.org/10.1088/1361-651X/ac11bc.
[39] A. Gupta, P.J. Zuk, H.A. Stone, Charging dynamics of overlapping double layers in a cylindrical nanopore, Phys. Rev. Lett. 125 (2020): 076001, https://doi.org/10.1103/PhysRevLett.125.076001.
[40] H. Wang, A. Thiele, L. Pilon, Simulations of cyclic voltammetry for electric double layers in asymmetric electrolytes: a generalized modified Poisson–Nernst–Planck model, J. Phys. Chem. C 117 (2013) 18286–18297, https://doi.org/10.1021/jp402181e.
[41] Y. Bu, H. Liang, R. Shi, H. Liu, Y. Zhang, T. Sun, C. Lian, X. Shen, H. Li, Assessing the maximum power and consistency of carbon supercapacitors through a facile practical strategy, ACS Sustain. Chem. Eng. 8 (2020) 12430–12436, https://doi.org/10.1021/acssuschemeng.0c03039.
[42] T.F. Fuller, M. Doyle, J. Newman, Simulation and optimization of the dual lithium ion insertion cell, J. Electrochem. Soc. 141 (1994) 1, https://doi.org/10.1149/1.2054684.
[43] B. Vijayaraghavan, D.R. Ely, Y.-M. Chiang, R. García-García, R.E. García, An analytical method to determine tortuosity in rechargeable battery electrodes, J. Electrochem. Soc. 159 (2012) A548, https://doi.org/10.1149/2.jes113224.
[44] M. Janssen, E. Griffioen, P.M. Biesheuvel, R. van Roij, B. Erné, Coulometry and calorimetry of electric double layer formation in porous electrodes, Phys. Rev. Lett. 119 (2017): 166002, https://doi.org/10.1103/PhysRevLett.119.166002.
[45] X. Wang, A.Y. Mehandzhiyski, B. Arstad, K.L. Van Aken, T.S. Mathis, A. Gallegos, Z. Tian, D. Ren, E. Sheridan, B.A. Grimes, D. Jiang, J. Wu, Y. Gogotsi, D. Chen, Selective charging behavior in an ionic mixture electrolyte-supercapacitor system for higher energy and power, J. Am. Chem. Soc. 139 (2017) 18681–18687, https://doi.org/10.1021/jacs.7b10693.
[46] Y. Gogotsi, P. Simon, True performance metrics in electrochemical energy storage, Science 334 (2011) 917–918, https://doi.org/10.1126/science.1213003.
[47] Z. Li, S. Gadipelli, H. Li, C.A. Howard, D.J.L. Brett, P.R. Shearing, Z. Guo, I. P. Parkin, F. Li, Tuning the interlayer spacing of graphene laminate films for efficient pore utilization towards compact capacitive energy storage, Nat. Energy 5 (2020) 160–168, https://doi.org/10.1038/s41560-020-0560-6.
[48] R. Drummond, C. Huang, P.S. Grant, S.R. Duncan, Overcoming diffusion limitations in supercapacitors using layered electrodes, J. Power Sources 433 (2019): 126579, https://doi.org/10.1016/j.jpowsour.2019.04.107.
[49] Q. Cheng, W. Chen, H. Dai, Y. Liu, X. Dong, Energy storage performance of electric double layer capacitors with gradient porosity electrodes, J. Electroanal. Chem. 889 (2021): 115221, https://doi.org/10.1016/j.jelechem.2021.115221.
[50] The Effect of Salt Concentration in Electrolytes on the Maximum Energy Storage for Double Layer Capacitors -, IOPscience 144 (1997) 2417–2420. https://iopscience.iop.org/article/10.1149/1.1837829.
[51] P. Huang, H. Tao, J. Yang, C. Lian, H. Liu, Four stages of thermal effect coupled with ion-charge transports during the charging process of porous electrodes, AIChE J. 68 (2022): e17790, https://doi.org/10.1002/aic.17790.
[52] W. Qu, D. Li, A model for overlapped EDL fields, J. Colloid Interface Sci. 224 (2000) 397–407, https://doi.org/10.1006/jcis.1999.6708.